Spatiotemporal Activity Patterns During Respiratory Rhythmogenesis in the Rat Ventrolateral Medulla

Jonathan A. N. Fisher, Vitaliy A. Marchenko, Arjun G. Yodh and Robert F. Rogers

Spatiotemporal Activity Patterns During Respiratory Rhythmogenesis in the Rat Ventrolateral Medulla

Jonathan A. N. Fisher,[1] Vitaliy A. Marchenko,[2] Arjun G. Yodh,[1] and Robert F. Rogers[2]
[1]*Department of Physics and Astronomy, University of Pennsylvania, Philadelphia, Pennsylvania; and* [2]*Department of Electrical and Computer Engineering, University of Delaware, Newark, Delaware*

Fisher, Jonathan A. N., Vitaliy A. Marchenko, Arjun G. Yodh, and Robert F. Rogers. Spatiotemporal activity patterns during respiratory rhythmogenesis in the rat ventrolateral medulla. *J Neurophysiol* 95: 1982–1991, 2006. First published December 7, 2005; doi:10.1152/jn.00674.2005. One of the most important brain rhythms is that which generates involuntary breathing movements. The lower brain stem contains neural circuitry for respiratory rhythm generation in mammals. To date, microsectioning and selective lesioning studies have revealed anatomical regions necessary for respiratory rhythmogenesis. Although respiratory neurons distributed within these regions can be identified by their firing patterns in different phases of the respiratory cycle, conventional electrophysiology techniques have limited the study of spatial organization within this network. Optical imaging techniques offer the potential for monitoring the spatiotemporal activity of large groups of neurons simultaneously. Using high-speed voltage-sensitive dye imaging and spatial correlation analysis in an arterially perfused in situ preparation of the juvenile rat, we determined the spatial distribution of respiratory neuronal activity in a region of the ventrolateral respiratory group containing the pre-Bötzinger complex (pBC) during spontaneous eupneic breathing. While distinctly pre- and postinspiratory-related responses were spatially localizable on length scales less than 100 μm, we found the studied area on whole exhibited a spatial mixture of phase-spanning and postinspiratory-related activity. Additionally, optical recordings revealed significant widespread hyperpolarization, suggesting inhibition in the same region during expiration. This finding is consistent with the hypothesis that inhibitory neurons play a crucial role in the inspiration-expiration phase transition in the pBC. To our knowledge this is the first optical imaging of a near fully intact in situ preparation that exhibits both eupneic respiratory activity and functional reflexes.

INTRODUCTION

Breathing is an essential function of all higher vertebrates. It is under both voluntary and involuntary control, with the involuntary component consisting of a basic rhythm generator within the CNS, with central and peripheral reflexive control elements. The neuronal center for generating rhythmic breathing in mammals is located in the medulla of the brain stem (Flourens 1851; Lumsden 1923; see Bianchi et al. 1995; Cohen 1981; von Euler 1986 for reviews). The neurons required for rhythmogenesis are localized primarily in a limited region of the ventrolateral medulla (Onimaru and Homma 2003; Smith et al. 1991), but their exact location and the mechanism of primary rhythm generation remains a subject of active inquiry.

Among these ventromedullary regions, the site known as the pre-Bötzinger complex (pBC) (Smith et al. 1991) is an important region for rhythmogenesis. This region contains many different respiratory neuron types (Schwarzacher et al. 1991; Sun et al. 1998) and has been established in vivo as essential for rhythmic breathing (Gray et al. 2001; Pierrefiche et al. 1998; Ramirez et al. 1998). While the exact nature of the mammalian breathing rhythm generator is not known, it is suspected that both intrinsic cellular and network properties contribute to rhythmogenesis with state-dependent (Rybak et al. 2002), and age-varying (Hilaire and Duron 1999; McCrimmon et al. 2000a,b; Paton et al. 1994) degrees of importance. Pharmacological studies in arterially perfused rats have revealed that synaptic inhibition is vital for respiratory rhythm generation in adults but not for neonates, suggesting an overall developmental shift in rhythmogenesis mechanism to a network mechanism (Hayashi and Lipski 1992; Paton et al. 1994). Many of these studies, however, are difficult to reconcile because each in vitro preparation defines a different operational condition compared with in vivo preparations (Richter and Spyer 2001). Clearly, there are differences in the generation of respiratory rhythm between neonates and adult rats, as well as between in vivo and in vitro models.

The pBC has been described in vitro as a major respiratory rhythm-generating region containing (early) inspiratory activity (Johnson et al. 2001; Koshiya and Smith 1999; Smith et al. 1991). On the other hand, in vivo electrophysiological study of the adult cat (Schwarzacher et al. 1995) and rat (Sun et al. 1998) has revealed that the pBC is a neuronally mixed area containing phase-spanning propriobulbar neurons that fire through the respiratory phase transition. These studies hypothesize that such phase-spanning neurons in the pBC promote the expiratory–inspiratory phase transition and are thus critical to rhythmogenesis in vivo. Thus results obtained in vivo versus in vitro suggest very different functional roles for the pBC.

To achieve a more global picture of neuronal distribution, some groups have used optical imaging techniques to visualize large-scale activity. Such studies, however, have concentrated on in vitro preparations of the neonatal rat, either of brain stem slices (Koshiya and Smith 1999; Tokumasu et al. 2001) or en bloc preparations of the brain stem and spinal cord (Onimaru and Homma 2003; Tokumasu et al. 2001). Unfortunately, interpretation of results from these neonatal or reduced preparations, with respect to adult in vivo mechanisms, incurs the same disadvantages described above.

We hypothesize that, in a more mature and intact rat preparation, the area of the pBC would be functionally mixed and exhibit significant activity throughout all phases of respiration, as in in vivo preparations. In addition, we expect that inhibitory mechanisms will be evident. To test this hypothesis, we used voltage-sensitive dye imaging to study the large-scale electrical spatiotemporal activity in the pBC area of a largely intact juvenile rat preparation. We performed high-speed wide-field fluorescence video microscopy of the surface of the medulla immediately ventral to the ventrolateral respiratory group (VRG) in an arterially perfused preparation of the juvenile rat (Paton 1996; St.-John and Paton 2000) using the voltage-sensitive dye di-8-ANEPPS. Using correlation coefficient analysis (Bandettini et al. 1993; Durduran et al. 2005), we identified nonoverlapping spatial regions within the pBC exhibiting fractional fluorescence signals at different phases of respiration.

A preliminary report of this work has been published in abstract form (Marchenko et al. 2004).

METHODS

General preparation

All procedures were performed with the approval of the University of Delaware Institutional Animal Care and Use Committee. Following the "working heart-brain stem preparation" (Paton 1996), juvenile rats (72–100 g; $n = 5$) were bisected just below the diaphragm, decerebrated at the precollicular level, and skinned under deep isoflurane anesthesia in 4°C artificial cerebrospinal solution. Deep anesthesia was assured by the absence of limb withdrawal and reflexive changes in breathing after limb pinch. They were bilaterally vagotomized, with the diaphragm, heart, lungs, and portions of the rib cage removed, and appropriate vasculature was ligated to prevent excessive leakage of the perfusate. The descending aorta was cannulated, and rats were perfused with a 95% O_2-5% CO_2-saturated solution consisting of 125 mM NaCl, 1.25 mM NaHCO$_3$, 4 mM KCl, 2.5 mM CaCl$_2$, 1.25 mM MgSO$_4$, 1.25 mM KH$_2$PO$_4$, 20 mM dextrose, 0.05 mg/ml vecuronium bromide, and 2.5% dextran (230 kDa) at 95–105 mmHg and gradually warmed to 31–33°C. This experimental preparation has been shown to produce eupneic breathing patterns in mice (Paton 1996) as well as rats (St.-John and Paton 2000).

Phrenic nerve (300–3,000 Hz) and single unit (500–3,000 Hz) recordings (10,000 samples/s) were made with silver wire hook electrodes and glass electrodes (2 M NaCl), respectively. Signals were amplified and filtered using conventional electronics (Neurolog, Digitimer). Raw phrenic nerve recordings were used to monitor the respiratory state of the preparation (e.g., eupnea, gasping) and to adjust perfusate flow accordingly.

Imaging system

Simultaneous image and electrophysiological data acquisition was performed with custom-built hardware (including camera) and custom-written software (Rector and George 2001; Rector et al. 1999, 2001) capable of continuous image and data recording at high speeds (up to 1-kHz frame rate for video data, 20 kHz/channel for electrophysiology data) for long periods of time (>1 h). The detector was a CCD camera (TC255, Texas Instruments, Dallas, TX; 10×10 μm pixels, 336×243 pixel array). To achieve appreciable signal levels, the frame rate was set to 100 Hz. The imaging optics consisted of a custom 1:1 focal length ratio lens couplet (Fig. 1A). Two identical achromatic lenses (Edmund Optics, Barrington, NJ) served as objective and focusing lenses. Light from a 200-W halogen white light source (Thermo Oriel, Newport Corp., Irvine, CA) was filtered with a

480 ± 20-nm excitation filter (Chroma Technology Corp., Rockingham, VT). The filtered light was coupled into the imaging device through a multimode fiber bundle that was recollimated with a collimating lens triplet (Melles Griot, Barloworld Scientific, Carlsbad, CA) and reflected off of a dichroic mirror (<500 nm R, Chroma Technology Corp.) to provide epi-illumination through the achromatic objective lens (Edmund Optics). The fluorescence signal was filtered with a >590-nm long-pass filter (Chroma Technology).

This relatively inexpensive optics configuration provides a large imaging area with sufficiently high numerical aperture (NA = 0.38) for voltage-sensitive dye fluorescence imaging. Additionally, the imaging device has a long working distance because of the large objective aperture. This allows for considerable electrophysiological, pharmacological, and surgical manipulation of the imaging area during recording, if necessary.

Dye staining

Stock solutions of voltage-sensitive dye di-8-ANEPPS dissolved in F-127 Pluronic (20% in DMSO; both from Molecular Probes/Invitrogen, Carlsbad, CA) were diluted to final concentrations of 500 μg/ml in Ringer solution. The diluted dye solution was loaded into the tissue systemically through a side port of the aortic perfusion line. After perfusion with di-8-ANEPPS, reduced rat preparations continued to exhibit eupneic breathing. In addition, it was possible to elicit the Hering-Breuer reflex—whereby inspiration is terminated and expiration extended—through electrical stimulation of the vagus nerve (Fig. 1B). We used the time latency and efficacy of the Hering-Breuer reflex and the overall phrenic activity (amplitude, duration, pattern, and rhythmicity) as indicators of possible toxic effects of systemic dye introduction. In all preparations, these parameters were not changed more than ±5% after 15–90 min of dye injection. In addition, the presence of stereotypical respiratory-related single-neuron activity (Fig. 1, C and D) provided further confidence that the effects of the dye-staining were inconsequential. Because the perfusate is optically transparent at the excitation and emission wavelengths (480 ± 20 and >590 nm, respectively) used in the experiment, erythrocyte-dependent, oxygenation-related optical artifacts, large sources of noise in in vivo conditions, were eliminated.

Measurement protocol

The imaged region included areas just rostral and lateral to the rostralmost XII rootlets, and the region indicated in Fig. 1A (rectangle) was used in all experiments. The focal plane of the camera was set to ~200 μm below the ventral surface. After the dye was loaded, raw images and electrophysiological data were collected for long durations (~40 min), during which several hundred eupneic breaths typically occurred. Triggered averaging of video and electrophysiology was performed off-line using custom written functions in Matlab software (MathWorks, Natick. MA). Integrated phrenic recordings ($\tau = 50$ ms) were used to create trigger markings for averaging, and the final processed data were averaged over 20–50 breaths. Off-line averaging enabled arbitrarily long pretrigger times. Because of the variability in phrenic burst duration, off-line triggered averaging was performed using both early- and late-phase triggering points. The onset of the integrated phrenic burst (defined by a threshold set just above the noise level) served as the "early" trigger point; the peak (i.e., turning point) of the integrated phrenic burst defined the "late" trigger point. For characterizing onset times and peak response values, early-phase triggered averaging was used for optical responses occurring just before the onset of the phrenic burst (preinspiratory period), and late-phase triggered averaging was used for responses during and after inspiration. Fractional fluorescence ($\Delta F/F$) images were produced by subtracting a reference image, F, from averaged video
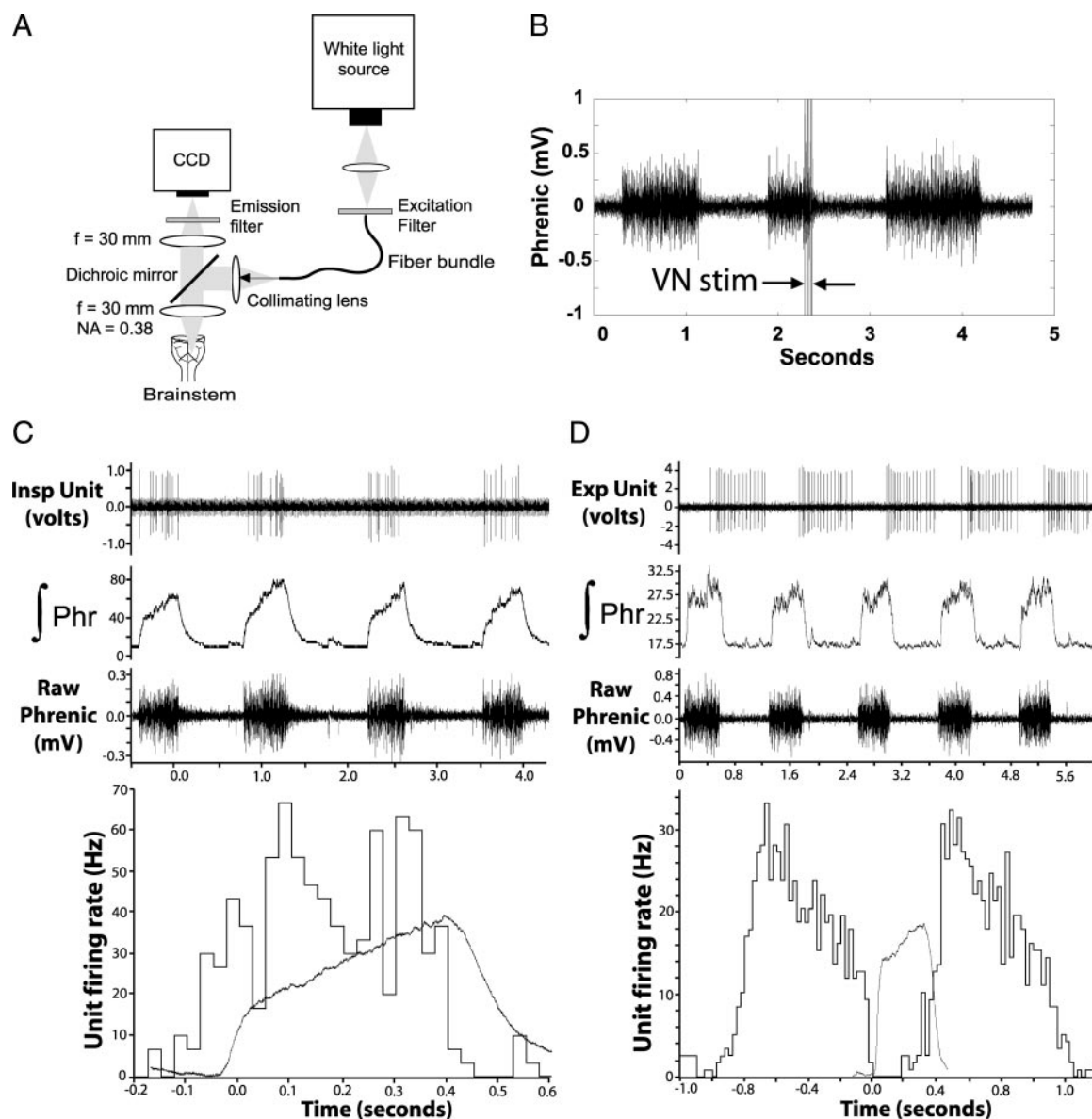
FIG. 1. Experimental system and physiological validation. *A*: optical setup for fluorescence measurements from the ventral medullary surface. *B*: Hering-Breuer reflex demonstration 15 min after injection of di-8-ANEPPS into perfusate. Region between arrows (VN stim) indicates electrical stimulation (0.2 ms, 50 Hz, 100 ms) of central end of transected cervical vagus nerve, leading to termination of inspiration (raw neurogram). *C* and *D*: single unit recordings of inspiratory (*C*) and expiratory (*D*) neurons in the pre-Bötzinger complex (pBC) region after injection of potentiometric dye. Traces from *top* in *C* and *D*: extracellular neurogram; integrated phrenic activity; raw phrenic neurogram; inspiratory cycle–triggered histogram of activity. Bin widths: 0.25 ms. Sweeps: $C = 32$, $D = 67$. Note time scales differ slightly in *C* and *D*.

images to generate ΔF. This quantity was divided by F to yield normalized changes and correct for irregularity in staining. Using our emission filter (>590 nm), di-8-ANEPPS exhibits a decrease in amplitude of fluorescence emission during membrane depolarization. Thus depolarizations are accompanied by negative changes in fractional fluorescence ($\Delta F/F$), and vice versa for membrane hyperpolarization. Fractional fluorescence CCD recordings were smoothed spatially with a 5×5 Gaussian filter and temporally with a five-frame sliding box car average. Other than this simple spatiotemporal smoothing, all data traces are presented unfiltered. After the imaging experiment, dye was preferentially applied to the two rostralmost XII rootlets by placing a small di-8-ANEPPS–saturated piece of gauze directly onto the rootlets with a pair of forceps for the purpose of generating a high-contrast background image including identifiable anatomical landmarks in the imaging field of view. After ~5 min, the gauze was removed, and unbound dye was washed away by the

constant outflow of perfusate in the brain stem area. Several seconds' worth of frames of this background were averaged to resolve anatomical details in the low-contrast tissue. Thresholded montage images (Fig. 2*C*) are displayed superimposed over this background image.

Image analysis

Voltage-sensitive dyes yield fluorescence changes linearly proportional to membrane potential changes and can therefore be used as a molecular voltmeters (Bullen and Saggau 1999; Cohen and Salzberg 1978; Salzberg 1983). However, because the polarity reported by $\Delta F/F$ depends on the choice of reference image, F, we compared $\Delta F/F$ using two different reference images. One reference image was generated by averaging the first 10 frames of the triggered average CCD recording. To achieve a reference fluorescence image more
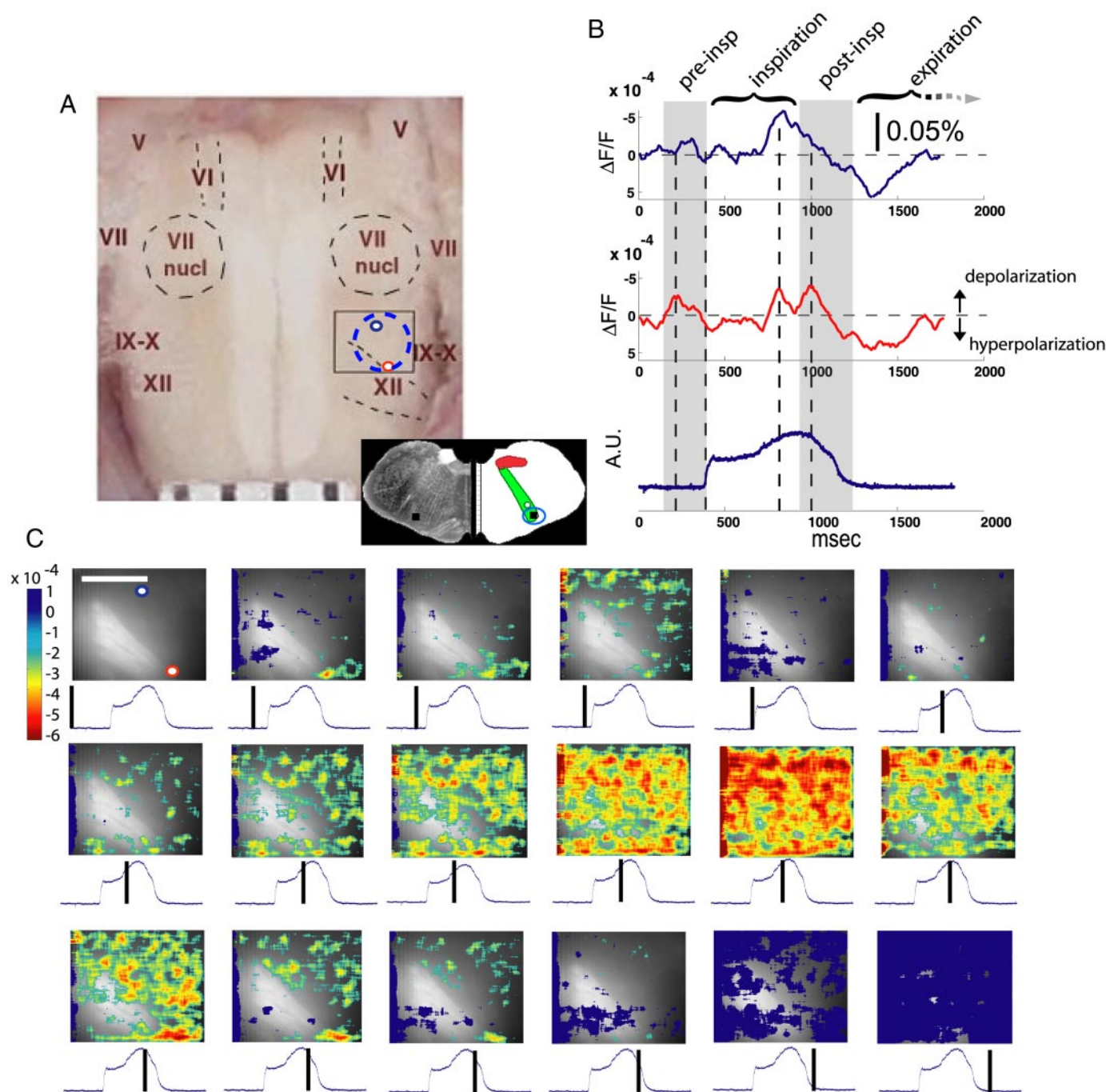
FIG. 2. Fluorescent respiratory-related signals from the rat ventrolateral medulla (VLM). *A*: anatomical location of imaged region. Rectangle outline indicates CCD imaging area. Dashed blue circle: approximate outline of pBC. Dashed lines: rostral and caudal limits of XII roots. Blue and red dots show locations used to generate corresponding traces in *B*. Scale bar, *bottom*, in mm. *Inset*: cross-sectional view taken from slice 1.05 mm rostral to calamus scriptorius. Red region: nucleus tractus solitarius. Green region: lateral tegmental field. Blue circle: pBC. Small square: approximate location of extracellular recordings in Fig. 1. *B*: *top* and *middle*: fractional fluorescence signal from corresponding points indicated in *A*. Note that axis scales have been inverted to mimic corresponding depolarization such that negative change in fractional fluorescence corresponds to an increase on these axes (i.e., depolarization). *Bottom*: corresponding averaged, integrated phrenic nerve activity plotted on same time scale. Shading: preinspiratory and postinspiratory portions of respiratory cycle. Dotted lines: relevant peaks in Δ*F/F*. *C*: montage of selected frames from a recording showing clear spatiotemporal separation of pre- and postinspiratory signals. Scale bar in 1st frame = 1 mm. Blue and red dots in 1st frame (same as in *A*) show regions of Δ*F/F* traces in *B*. Images are superimposed on background fluorescence image displaying 2 rostralmost XII rootlets. Below each frame is integrated phrenic trace with a time marker (vertical bar) representing the temporal relationship of current frame with respect to respiratory cycle. Note emerging widespread excitation during inspiration (*2nd row*) and widespread inhibition during expiration (*bottom row*).

likely close to steady-state potentials, the preparation was cooled to a temperature of 16°C, during which no rhythmic or tonic phrenic activity was observed and fluorescence images were recorded and averaged to generate *F*.

Correlation coefficient images (Bandettini et al. 1993; Durduran et al. 2005) were computed by calculating the correlation coefficient for each pixel with a given correlation function. The correlation coefficient, cc_i, is defined as

$$cc_i = \frac{\sum_{n=1}^{N}(f_i - \mu_f)(r_i - \mu_r)}{\sqrt{\sum_{n=1}^{N}(f_i - \mu_f)^2}\sqrt{\sum_{i=1}^{N}(r_i - \mu_r)^2}} \qquad (1)$$

where f_i ($i = 1 \ldots N$) is the time-course of $\Delta F/F$ for a given pixel, r_i ($i = 1 \ldots N$) is the function representing the desired correlation function during respiration, μ_f and μ_r are the mean values of f and r, and N is the number of frames.

Two types of functions were used in our correlation analysis: functions that approximate firing frequency rates for five basic types of respiratory neurons (preinspiratory, late-inspiratory, postinspiratory, ramp-inspiratory, and expiratory-augmenting) and functions that approximate the membrane potential trajectories for those same neuron types. Approximations were based on descriptions by Bianchi et al. (1995). Following the description of the respiratory phases in Richter et al. (1986), three points on the integrated phrenic burst recording were used to define the inspiratory and expiratory phases (Fig. 2B) and to define correlation functions (Fig. 3A): the onset of the inspiratory phrenic burst, the peak/turning point of the inspiratory phrenic trace, and the return to baseline of the phrenic trace. The period of "inspiration" spanned the duration between the phrenic burst onset point and the peak/turning point. "Postinspiration" (i.e., E1) was defined as the period between the integrated phrenic peak/turning point and the return to baseline of the phrenic trace. "Expiration" (i.e., E2), spanned the duration between the return to baseline of the integrated phrenic trace and the onset of the next breath's phrenic burst.

Because depolarization resulted in a negative change in fluorescence while the value of correlation functions followed the sign convention of intracellular neuron recordings (depolarization represented by a positive change), maximal cc values are negative when the sign of the correlation function is opposite that of the optical response. A $|cc|$ value of 1 would imply that the time-course of $\Delta F/F$ is identical to the correlation function multiplied by an arbitrary constant; a $|cc|$ value of 0 indicates no similarity between the $\Delta F/F$ time-course and the correlation function. Maximum values of $|cc|$ for our data ranged from 0.4 to 0.7, because of mismatch between model functions and real activity and the presence of physiological and CCD noise in optical recordings.

RESULTS

For all rats ($n = 5$) in a region that included the pBC, we observed consistent fractional fluorescence responses during the preinspiratory period, inspiration, postinspiration, and expiration (see METHODS for detailed definition of periods). The fractional fluorescence responses during preinspiration, inspiration, and postinspiration were all statistically significant negative changes in fluorescence, indicating depolarization (Fig. 2B). The fractional fluorescence response during expiration was a statistically significant increase in fluorescence, indicating hyperpolarization (Fig. 2B). While peak response regions were spatially localizable on length scales less than 100 μm, all optical responses were readily detectible in time traces of $\Delta F/F$ averaged over the entire field of view.

Averaging over all animals, the integrated phrenic burst duration, defined here as the time between the onset and the return to baseline of the phrenic burst, was 935 ± 68 (SD) ms. The range of breath durations was between 870 and 1,000 ms and the SD of the phrenic burst duration was <9% within individual experiments. Because of the variability in phrenic burst duration, onset times (in ms) of optical responses will be described both in terms of mean $\pm$ SD (averaging over all animals) and in terms of percentages of the inspiratory burst duration (i.e., onset values are divided by individual experiment phrenic burst duration before group averaging) to give more qualitatively general descriptions. As described in METHODS, the variability in phrenic burst durations necessitated the use of early- and late-phase triggered averaging. Averaging using either trigger points did not erase any of the responses but did lead to smaller SD when the trigger closest to the optical response was used. The "preinspiratory" response onset preceded the phrenic burst onset by 178 ± 85 ms or $19 \pm 9\%$ of the phrenic burst duration. This initial gross fluorescence response had an average peak value of $-0.029 \pm 0.014\%$ and always ended before the middle of inspiration. The $\Delta F/F$ response (triggered off of the onset of inspiration) that peaked during inspiration began 296 ± 107 ms ($27 \pm 9\%$) after the phrenic burst onset and reached peak values of $-0.037 \pm 0.015\%$. The $\Delta F/F$ response (triggered off of the phrenic peak) that reached maximum during the postinspiratory period (e.g., Fig. 2B, last peak in red trace) began 329 ± 174 ms before the phrenic burst peak ($29 \pm 12\%$ of the burst width), and reached $\Delta F/F$ values of $-0.038 \pm 0.024\%$. We found a small but significant overall increase in fluorescence of $+0.023 \pm 0.020\%$ during the expiratory period, indicating hyperpolarization (Fig. 2C; note the graph scales and color bars have been inverted so a decrease in fluorescence indicates membrane depolarization).

Using either the average of the first 10 triggered-average frames or the average of 10 random frames in a continuous fluorescence recording of the cooled brain stem (of the same preparation), the pre- and late-inspiratory $\Delta F/F$ changes were negative, indicating widespread depolarization (e.g., Fig. 2C, middle row, last 2 frames). In addition, using the cooled-brain stem fluorescence signal (no phrenic activity) as a baseline, F, revealed gross depolarization during the presence of tonic activity (data not shown).

On the scale of our field of view ($\sim 1 \times 1.2$ mm), we were able to distinguish both global and spatially localized phasic $\Delta F/F$ responses without the aid of image processing. Figure 2B shows $\Delta F/F$ responses at two different locations within the field of view. The top trace (blue) shows the $\Delta F/F$ time trace from the blue marker on the field of view in Fig. 2A. While this trace is representative of the gross postinspiratory $\Delta F/F$ changes seen in the frame montage in Fig. 2C, the red trace in Fig. 2B, corresponding to the area near the rostral-most XII rootlet (Fig. 2A, red dot), shows an additional pre- and postinspiratory signal not present in other regions. Figure 2C shows the typical degree of spatiotemporally restricted fluorescence changes from the region over the course of a breath.

While some spatiotemporal variations were apparent without any image processing, other features could be identified through correlation coefficient imaging. Figure 3 shows the results of correlation coefficient analysis using functions approximating both firing frequency and membrane potential patterns for five basic respiratory neuron types. The histograms in Fig. 3, A and B, represent correlation coefficients of all pixels in all experiments, using both early- and late-phase triggered averaging. Some of the histograms have one main peak, whereas others are clearly multimodal, indicating high or low consistency among experiments, respectively. Early- and late-phase triggered averaging revealed differences in this spread of correlation values; triggered averaging led to a decrease in the cc value spread when the selected trigger event
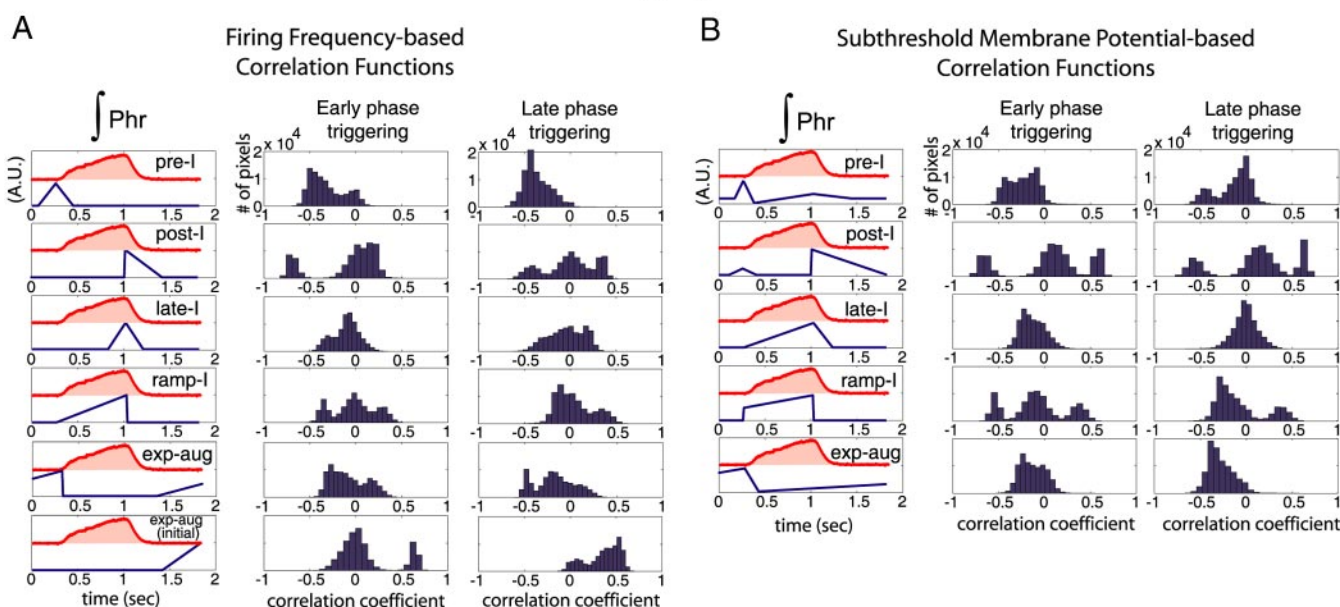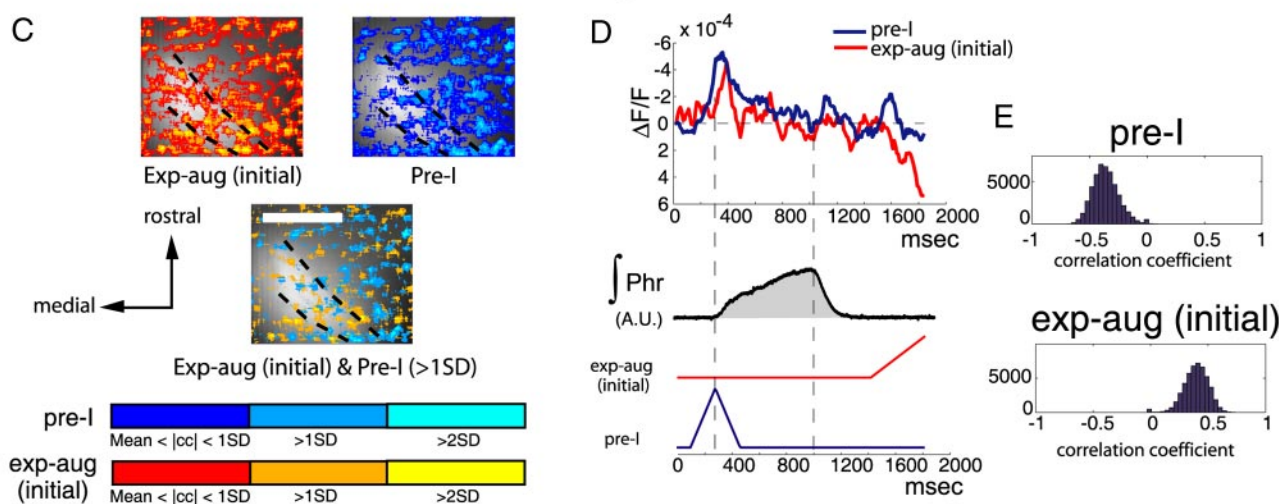
FIG. 3. Spatiotemporal correlation analysis of activity. *A*: correlation analysis (over all experiments) using firing frequency-based correlation functions. *A*: *left*: averaged integrated phrenic (∫Phr) trace (red) shown along with each different correlation function based on the firing-frequency traces of respiratory neurons (blue). *Middle*: histograms of calculated pixel correlation coefficients (for all experiments) based on the correlation function (blue) on the *left* using phrenic onset-triggered averaging (early-phase triggering). *Right*: histograms of calculated pixel correlation coefficients (based on the same correlation functions as *middle*) using phrenic peak-triggered averaging (late-phase triggering). *B*: correlation analysis (over all experiments) using subthreshold membrane potential-based correlation functions. *B*: *left*: averaged integrated phrenic (∫Phr) trace (red) shown along with each different correlation function based on subthreshold membrane potential traces of respiratory neurons (blue). *Middle*: histograms of calculated pixel correlation coefficients based on the correlation function (blue) on the *left* using early-phase triggered averaging. *B*: *Right*: histograms of calculated pixel correlation coefficients (based on the same correlation functions as *middle*) using late-phase triggered averaging. *C*: *top 2 images*: sample images of highly correlated regions for expiratory-augmenting [exp-aug (initial), blue-cyan colorbar] and preinspiratory (preI, red-yellow colorbar) firing frequency-based correlation functions (shown at the *bottom* of *D*) in a single experiment. Color bar below defines 3 ranges of correlation coefficient (*cc*) values: (Mean *cc* value) < |*cc*| < 1 SD, |*cc*| > 1 SD, |*cc*| > 2 SD. Correlation regions are thresholded as indicated by color bar. Mean *cc* values and SD are derived from Gaussian fits of *cc* value histograms (shown in *E*). Images are superimposed on fluorescence background image of di-8-ANEPPS–labeled XII rootlets; scale bar = 0.5 mm. Dotted lines: outline of 2 rostralmost XII rootlets. *Bottom*: combined correlation regions showing only |*cc*| values >1 SD. *D*: *top*: color-coded region-averaged time traces corresponding to regions in *C*. Traces represent averaged activity in all pixels with values of |*cc*| >2 SD of the mean *cc* value. *Bottom*: corresponding averaged, integrated phrenic recording used in *C* and *D*. Color-coded functions below phrenic show firing frequency-based functions used in correlation analysis for *C*. *E*: histograms of pixel *cc* values for individual experiment analysis.

was near the main feature (if any) of the correlation function (e.g., pre-*I* pattern using phrenic onset triggering). Because of this triggering-dependent effect, we additionally analyzed correlation statistics for the initial portion (beginning immediately after the return of the integrated phrenic trace to baseline) of the expiratory-augmenting firing frequency function, which has main features coincident with both early and late trigger events. For both firing frequency and membrane potential

functions, the least experimental variability was observed in the correlation analysis using preinspiratory (pre-*I*), late-inspiratory (late-*I*), and initial expiratory-augmenting [exp-aug (initial)] functions (functions shown in *left columns* of Fig. 3, *A* and *B*). Of those, pre-*I* and exp-aug (initial) firing-frequency functions revealed nonzero mean $|cc|$ values, indicating some degree of similarity to those functions among pixels in all experiments. A negative mean *cc* value was observed among experiments to the pre-*I* firing-frequency correlation function, and a positive mean *cc* value was observed using the exp-aug firing frequency function, interpreted as depolarization and hyperpolarization in those temporal patterns, respectively. Compared with the truncated exp-aug (initial) function, the full exp-aug correlation function revealed considerable experimental variability and no significant nonzero mean *cc* value.

Examination of an individual experiment (Fig. 3, *C–E*) reveals a spatial mixture of regions correlated with significantly different functions. The top two images in Fig. 3*C* show a thresholded map of *cc* values for pre-*I* and exp-aug (initial) correlation functions and reveal that both regions of high correlation cover a similar portion of the field of view. The bottom image in Fig. 3*C* displays the combined regions of the top two images (minimum threshold set to 1 SD of the mean $|cc|$ value), showing that the highly correlated ($|cc| > 2$ SD) subregions are largely nonoverlapping. For all experiments, there was <5% overlap for regions with $|cc|$ values >2 SD for pre-*I* and exp-aug firing-frequency functions, indicating spatial separation between the regions with the strongest temporal correlations.

Region-averaged plots of $\Delta F/F$ (Fig. 3*D*) revealed that $|cc|$ values larger than 2 SD showed significantly different time traces for the two correlation functions. While the region-averaged plot of pre-*I*-correlated activity did not exhibit the exp-aug (initial) characteristic increase in fluorescence (note again the reversed *y*-axis), some degree of pre-*I*–like $\Delta F/F$ response (peak at ~300 ms; Fig. 3*D*) was seen in pixels highly correlated with the exp-aug function. Additionally, similar to the traces in Fig. 2*B* (in a different experiment), the pre-*I*–correlated region contained smaller optical responses in the postinspiratory and expiratory periods.

During simultaneous optical recordings, we recorded extracellularly from 13 neurons that exhibited respiratory phase-related activity, all in the CCD field of view and within 340 μm from the ventral surface. Among these, were neurons with pre-*I* activity (onset of activity 65.2 ± 8.4 ms before phrenic onset with maximum firing frequency at the phrenic onset), early-*I,* and late-*I* activity (frequency peaks; see Fig. 1*C* for examples). In regions exhibiting post-*I* activity, several expiratory-decrementing units were also found (onset of activity ~ midinspiration; max firing at phrenic post-*I* onset). Figure 1*D* shows an example of one of these units. Thus neurons with or without "prototypical" firing patterns for a given region may be observed within that region, indicating a fair amount of spatial mixture, particularly on scales >200 μm.

DISCUSSION

In efforts to dissect the underlying mechanisms of respiratory rhythmogenesis, different in vitro preparations have been developed and each has its own particular rhythmic properties that differ from an in vivo preparation (Richter and Spyer

2001). Ramping, eupneic integrated phrenic recordings combined with the ability to elicit the Hering-Breuer reflex in this artificially perfused preparation (even after the injection of voltage-sensitive dye di-8-ANEPPS into the circulatory system) suggests superior degrees of functional relevance compared with brain stem/spinal cord en bloc or in vitro medullary slice preparations. The results clearly show the feasibility and use of optical imaging of the working heart–brain stem preparation via voltage-sensitive dyes. We also showed that the components of an important portion of the rhythm generator may be spatiotemporally characterized using these methods. This represents the first step in dissecting this system as it functions in its intact form, with the ultimate goal of creating a realistic quantitative model.

This is the first study, to our knowledge, to show correlation in subregions of the optical image to specific known firing patterns of respiratory neurons in a relatively intact preparation. The results shown in Figs. 2 and 3 suggest that the $\Delta F/F$ response in the area of the pBC can be divided into at least four periods of response: preinspiratory, inspiratory, postinspiratory, and expiratory. The presence of $\Delta F/F$ signals during all four of these periods is fully consistent with recent voltage-sensitive dye imaging results in the brain stem–spinal cord preparation (Onimaru and Homma 2003) and with known membrane-potential dynamics for respiratory neuron types (Bellingham 1998; Ezure et al. 1988; Hayashi et al. 1996; Richter 1996; Rybak et al. 1997a).

Several reports have found that among neighboring regions in the VRG, the pBC is a region containing a relatively high variety of respiratory neuron types including pre-*I*, post-*I*, phase-spanning, and exp-2 neuron types (Ezure et al. 2003b; Howard and Tabatabai 1975; Sun et al. 1998). While it was apparent that distinctly preinspiratory and postinspiratory $\Delta F/F$ responses could be spatially distinguished within our imaging field of view (Fig. 2), the largest homogeneous subregions observed in one experiment were ~400 μm in diameter. Additionally, correlation coefficient images showed that regions exhibiting strong preinspiratory $\Delta F/F$ signals also exhibited significant postinspiratory activity (Fig. 3*D*, blue trace with small peak at post-*I* onset), akin to recent optical imaging studies of the ventral surface of the para-facial respiratory group (pFRG) (Onimaru and Homma 2003). Our findings are therefore in agreement with the model of the rat pBC as a region consisting of predominantly mixed neuron types and involved in phase-transition (Sun et al. 1998).

The results of correlation coefficient image analysis revealed widespread correlation of the optical signal with pre-*I* and exp-aug (initial) firing-frequency functions. The least speculative interpretation of this finding is that the optical signal tended to take on the same general form as those particular functions. The extent to which this finding depends on integration time remains unclear and is beyond the scope of this study.

Our findings of significant increase in fluorescence, corresponding to hyperpolarization, directly after the termination of inspiration in a region containing the pBC represent the first optical imaging evidence in support of the prevalence of inhibitory activity during rhythmogenesis. Glycinergic inhibition of distinct subsets of respiratory neurons in the VRG has been increasingly identified as crucial for respiratory rhythmogenesis (Busselberg et al. 2001a,b; Dutschmann and Paton

2002; Ezure et al. 2003a; Markstahler et al. 2001). The region of the pBC, specifically, has been shown pharmacologically to be rich in glycine receptors (Chitravanshi and Sapru 2002). That similar increases in fluorescence were not seen in previous imaging studies of the brain stem–spinal cord preparation (Onimaru and Homma 2003; Tokumasu et al. 2001) suggests further functional differences between neonatal in vitro and our juvenile in situ preparations.

The measurements in this report used linear (one-photon) fluorescence. Thus the contribution of out-of-focus light and scattering of the returning fluorescence must be considered. Voltage-sensitive dyes exhibit linear changes in fluorescence and absorption spectra as a function of membrane potential, but the definite spatial and temporal localization of the signal depend on the collection optics and integration time, respectively. Our system specifications (integration time = 8 ms; NA = 0.38) enabled us to discern fast optical signals with a wide field-of-view and long working distance. These specifications lead to uncertainty in both temporal and spatial localization of the signal origins. The observed signal at each pixel represents a spatial and temporal summation of the fluorescence activity in all of the stained membrane surface area contained within the volume defined by the lateral width (10 × 10 μm) and by the fluorescence depth-of-field (~10 μm). Calibration tests with fluorescent polystyrene beads placed at varying degrees of defocus show that the optical signal at each pixel reflects fluorescence from up to approximately ±50 μm surrounding the focal plane (Fisher et al. 2004).

Because the optical signal at each pixel represents a summation over a potentially unknown distribution of membrane area, the electrophysiological interpretation of the voltage-sensitive dye signal warrants further discussion. High-speed microscopy using voltage-sensitive dyes can provide optical recordings identical to all excitable membranes in the cellular architecture (including pre- and postsynaptic elements, somata, glia, etc; Konnerth and Orkand 1986; Konnerth et al. 1987). However, studies in which single detector pixels correspond to a mixture of neuronal architecture have found that voltage-sensitive dye measurements largely reflect a superposition of subthreshold membrane potential dynamics rather than spiking (Grinvald et al. 1982; Kleinfeld and Delaney 1996; Kleinfeld et al. 1994; Tokumasu et al. 2001). Other voltage-sensitive dye studies using spike-triggered imaging found that the optical signal was most similar to local field potential (LFP) measurements (Arieli et al. 1995; Grinvald et al. 1994), further concluding that the optical signal likely reflects primarily dendritic synaptic potentials rather than spiking. Unfortunately, the basic respiratory neurons are not nearly as well characterized in terms of their dendritic electrical properties as they are in terms of spiking behavior. Likewise, there is less certainty about the consistency of subthreshold membrane potential dynamics of respiratory neurons than of firing frequency. The best interpretation of our imaging results therefore is as indicative of summed membrane potential dynamics.

Because the imaged plane was ~200 μm below the ventral surface of the brain stem, scattering of the returning fluorescence signal can be expected to account for some further loss of spatial resolution. In the rat brain stem, the scattering properties increase significantly after 3 weeks of life because of increased myelination (Kasparov et al. 2002). To avoid this potential limitation, our study used rats just less than 3 weeks old. Taking into account the absence of blood in the artificially perfused preparation, as well as the fact that in vitro scattering coefficient values are almost always higher than in vivo values in brain tissue (Bevilacqua et al. 1999), it is reasonable to assume that there are relatively few scattering events in the first few hundred micrometers of tissue.

In light of these interpretive issues associated with the optical response, the thresholded regions in Fig. 2 and the significantly correlated regions in Fig. 3 should not necessarily be interpreted as the locations of cell bodies. Respiratory neurons in the VRG send their axonal projections and branching collaterals over large distances, frequently exceeding a diameter of several millimeters (Ezure 1990). A large fraction of the resulting $\Delta F/F$ signal likely contains contributions from portions of neurons other than the somata, particularly from the dendrites, which contain a large fraction of the surface area of these neurons (Ezure 1990). Overall, our results show that the area of the pBC contains spatially mixed subregions that exhibit optical responses during all phases of respiration, and that those subregions' optical responses exhibit further similarities to the electrical properties of specific respiratory neuron types. These results suggest that even at the juvenile developmental stage, the pBC region already shows stereotypical network-driven phenomena (i.e., widespread inhibition), and may participate in the generation of respiratory phase transitions.

In conclusion, our findings support the model of the pBC in the juvenile rat as a network of neurons that is spatially mixed in its organization, but with identifiable substructural organization that receives near-global excitatory and inhibitory influences during inspiration and expiration, respectively. In addition, the subregions that show the strongest pre-*I* and E-aug correlations are not spatially overlapping. We expect the methods used herein will lead to higher-resolution qualitative and quantitative models of the respiratory rhythm generator.

R E F E R E N C E S

Arieli A, Shoham D, Hildesheim R, and Grinvald A. Coherent spatiotemporal patterns of ongoing activity revealed by real-time optical imaging coupled with single-unit recording in the cat visual cortex. *J Neurophysiol.* 73: 2072–2093, 1995.

Bandettini PA, Jesmanowicz A, Wong EC, and Hyde JS. Processing strategies for time-course data sets in functional MRI of the human brain. *Mag Res Med* 30: 161–173, 1993.

Bellingham MC. Driving respiration: the respiratory central pattern generator. *Clin Exp Pharmacol Physiol* 25: 847–856, 1998.

Bevilacqua F, Piguet D, Marquet P, Gross JD, Tromberg BJ, and Depeursinge C. In vivo local determination of tissue optical properties: applications to human brain. *Appl Optics* 38: 4939–4950, 1999.

Bianchi AL, Denavit-Saubié M, and Champagnat J. Central control of breathing in mammals: neuronal circuitry, membrane properties, and neurotransmitters. *Phys Rev* 75: 1–45, 1995.

Bullen A and Saggau P. High-speed, random-access fluorescence microscopy: II. Fast quantitative measurements with voltage-sensitive dyes. *Biophys J* 76: 2272–2287, 1999.

Busselberg D, Bischoff AM, Becker K, Becker CM, and Richter DW. The respiratory rhythm in mutant oscillator mice. *Neurosci Lett* 316: 99–102, 2001a.

Busselberg D, Bischoff AM, Paton JF, and Richter DW. Reorganisation of respiratory network activity after loss of glycinergic inhibition. *Pflugers Arch* 441: 444–9, 2001b.

Chitravanshi VC and Sapru HN. Microinjections of glycine into the pre-Bötzinger complex inhibit phrenic nerve activity in the rat. *Brain Res* 947: 25–33, 2002.

Cohen MI. Central determinants of respiratory rhythm. *Ann Rev Physiol* 43: 91–104, 1981.

Cohen LB and Salzberg BM. Optical measurement of membrane potential. *Rev Physiol Biochem Pharmacol* 83: 35–88, 1978.

Del Negro CA, Morgado-Valle C, and Feldman JL. Respiratory rhythm: an emergent network property? *Neuron* 34: 832–830, 2002.

Durduran T, Burnett MG, Yu G, Zhou C, Furuya D, Yodh AG, Detre JA, and Greenberg JH. Spatiotemporal quantification of cerebral blood flow during functional activation in rat somatosensory cortex using laser-speckle flowmetry. *J Cereb Blood Flow Metab* 24: 518–525, 2005.

Dutschmann M and Paton JFR. Glycinergic inhibition is essential for co-coordinating cranial and spinal respiratory motor outputs in the neonatal rat. *J Physiol* 532. 2: 643–653, 2002.

Ezure K. Synaptic connections between medullary respiratory neurons and considerations on the genesis of respiratory rhythm. *Prog Neurobiol* 35: 429–450, 1990.

Ezure K, Manabe M, and Yamada H. Distribution of medullary respiratory neurons in the rat. *Brain Res* 455: 262–270, 1988.

Ezure K, Tanaka I, and Kondo M. Glycine is used as a transmitter by decrementing expiratory neurons of the ventrolateral medulla in the rat. *J Neurosci* 23: 8941–8948, 2003a.

Ezure K, Tanaka I, and Saito Y. Activity of brainstem respiratory neurons just before the expiration-inspiration transition in the rat. *J Physiol* 547: 629–640, 2003b.

Feldman JL. Neurophysiology of breathing in mammals. In: *Handbook of Physiology. The Nervous System. Intrinsic Regulatory System in the Brain*, edited by Bloom FE. Washington, DC: American Physiological Society, 1986, p. 463–524.

Fisher JAN, Civillico EF, Contreras D, and Yodh AG. In vivo fluorescence microscopy of neuronal activity in three-dimensions by use of voltage-sensitive dyes. *Optics Lett* 29: 71–73, 2004.

Flourens MJP. Note sur le point vital de la moelle allongée. *C R Seances Soc Biol* 33: 437–439, 1851.

Gray PA, Janczewski WA, Mellen N, McCrimmon DR, and Feldman JL. Normal breathing requires preBotzinger complex neurokinin-1 receptor-expressing neurons. *Nat Neurosci* 4: 927–930, 2001.

Grinvald A, Lieke EE, Frostig RD, and Hildesheim R. Cortical point-spread function and long-range lateral interactions revealed by real-time optical imaging of Macaque monkey primary visual cortex. *J Neurosci* 14: 2545–2568, 1994.

Grinvald A, Manaker A, and Segal M. Visualization of the spread of electrical activity in rat hippocampal slices by voltage sensitive optical probes. *J Physiol* 333: 269–291, 1982.

Hayashi F, Coles SK, and McCrimmon DR. Respiratory neurons mediating the Breuer-Hering reflex prolongation of expiration in rat. *J Neurosci* 16: 6526–6536, 1996.

Hayashi F and Lipski J. The role of inhibitory amino acids in control of respiratory motor output in an arterially perfused rat. *Respir Physiol* 89: 47–63, 1992.

Hilaire G and Duron B. Maturation of the mammalian respiratory system. *Physiol Rev* 79: 325–360, 1999.

Howard BR and Tabatabai M. Localization of the medullary respiratory neurons in rats by microelectrode recording. *J Appl Physiol* 39: 812–817, 1975.

Johnson SM, Koshiya N, and Smith JC. Isolation of the kernel for respiratory rhythm generation in a novel preparation: The pre-Bötzinger complex "island" *J Neurorphysiol* 1772–1776, 2001.

Kashiwagi M, Onimaru H, and Homma I. Correlation analysis of respiratory neuron activity in ventrolateral medulla of brainstem-spinal cord preparation isolated from newborn rat. *Exp Brain Res* 95: 277–290, 1993.

Kasparov S, Teschemacher AG, and Paton JFR. Dynamic confocal imaging in acute brain slices and organotypic slice cultures using a spectral confocal microscope with single photon excitation. *Exp Physiol* 87: 715–724, 2002.

Kleinfeld D and Delaney KR. Distributed representation of vibrissa movement in the upper layers of somatosensory cortex revealed with voltage-sensitive dyes. *J Comp Neurol* 375: 89–108, 1996.

Kleinfeld D, Delaney KR, Fee MS, Flores JA, Tank DW, and Gelperin A. Dynamics of propagating waves in the olfactory network of a terrestrial mollusc: an electrical and optical study. *J Neurophysiol* 72: 1402–1419, 1994.

Konnerth A, Obaid AL, and Salzberg BM. Optical recording of electrical activity from parallel fibres and other cell types in skate cerebellar slices in vitro. *J Physiol* 393: 681–702, 1987.

Konnerth A and Orkand RK. Voltage-sensitive dyes measure potential changes in axons and glia of the frog optic nerve. *Neurosci Lett* 66: 49–54, 1986.

Koshiya N and Smith JC. Neuronal pacemaker for breathing visualized in vitro. *Nature* 400: 360–363, 1999.

Lumsden T. Observations on the respiratory centers in the cat. *J Physiol* 57: 153–160, 1923.

Marchenko VA, Fisher JAN, Rector DM, Yodh AG, and Rogers RF. Optical recording of respiratory-related activity from the ventrolateral medulla of artificially perfused juvenile rats. *Soc Neurosci Abstr* 187.1, 2004.

Markstahler U, Kremer E, Kimmina S, Becker K, and Richter DW. Effects of functional knock-out of α_1 glycine-receptors on breathing movements in *oscillator* mice. *Respir Physiol Neurobiol* 130: 33–42, 2001.

McCrimmon DR, Monnier A, Hayashi F, and Zuperku EJ. Pattern formation and rhythm generation in the ventral respiratory group. *Clin Exp Pharmacol Physiol* 27: 126–131, 2000a.

McCrimmon DR, Ramirez J-M, Alford S, and Zuperku EJ. Unraveling the mechanism for respiratory rhythm generation. *BioEssays* 22: 6–9, 2000b.

Onimaru H and Homma I. A novel functional neuron group for respiratory rhythm generation in the ventral medulla. *J Neurosci* 23: 1478–1486, 2003.

Onimaru H, Kanamaru A, and Homma I. Optical imaging of respiratory burst activity in newborn rat medullary block preparations. *Neurosci Res* 25: 183–90, 1996.

Paton JF, Ramirez JM, and Richter DW. Mechanisms of respiratory rhythm generation change profoundly during early life in mice and rats. *Neurosci Lett* 170: 167–70, 1994.

Paton JFR. A working heart-brainstem preparation of the mouse. *J Neurosci Methods* 65: 63–68, 1996.

Pierrefiche O, Schwarzacher SW, Bischoff AM, and Richter DW. Blockade of synaptic inhibition within the pre-Botzinger complex in the cat suppresses respiratory rhythm generation in vivo. *J Physiol* 1: 245–254, 1998.

Ramirez JM, Schwarzacher SW, Pierrefiche O, Olivera BM, and Richter DW. Selective lesioning of the cat pre-Botzinger complex in vivo eliminates breathing but not gasping. *J Physiol* 507. 3: 895–907, 1998.

Rector DM and George JS. Continuous image and electrophysiological recording with real-time processing and control. *Methods* 25: 151–163, 2001.

Rector DM, Rogers RF, and George JS. A focusing image probe for detecting neural activity in vivo. *J Neurosci Methods* 91: 135–145, 1999.

Rector DM, Rogers RF, Schwaber JS, Harper RM, and George JS. Scattered light imaging in vivo tracks fast and slow processes of neurophysiological activation. *NeuroImage* 14: 977–994, 2001.

Rekling JC and Feldman JL. Prebotzinger complex and pacemaker neurons: hypothesized site and kernel for respiratory rhythm generation. *Annu Rev Physiol* 60: 385–405, 1998.

Richter DW. Neural regulation of respiration: rhythmogenesis and afferent control. In: *Comprehensive Human Physiology,* vol. II, edited by Greger R and Windhorst U. Berlin: Springer-Verlag, 1996, p. 2079–2095.

Richter DW, Ballantyne D, and Remmers JE. How is the respiratory rhythm generated? A model. *News Physiol Sci* 1: 109–112, 1986.

Richter DW and Spyer KM. Studying rhythmogenesis of breathing: comparison of in vivo and in vitro models. *Trends Neurosci* 24: 262–472, 2001.

Rybak IA, Paton JFR, Rogers RF, and St.-John WM. Generation of the respiratory rhythm: state-dependency and switching. *Neurocomputing 44-46*: 605–614, 2002.

Rybak IA, Paton JFR, and Schwaber JS. Modeling neural mechanisms for genesis of respiratory rhythm and pattern. I. Models of respiratory neurons. *J Neurophysiol* 77: 1994–2006, 1997a.

Rybak IA, Paton JFR, and Schwaber JS. Modeling neural mechanisms for genesis of respiratory rhythm and pattern. II. Network models of the central respiratory pattern generator. *J Neurophysiol* 77: 2007–2026, 1997b.

Salzberg BM. Optical recording of electrical activity in neurons using molecular probes. In: *Current Methods in Cellular Neurobiology*, edited by Barker J and McKelry J. New York: John Wiley, 1983, p. 139–187.

Schwarzacher SW, Smith JC, and Richter DW. Pre-Botzinger complex in the cat. *J Neurophysiol* 73: 1452–1461, 1995.

Schwarzacher SW, Wilhelm Z, Anders K, and Richter DW. The medullary respiratory network in the rat. *J Physiol* 435: 631–644, 1991.

Smith JC, Ellenberger HH, Ballanyi K, Richter DW, and Feldman JL. Pre-Botzinger complex: a brainstem region that may generate respiratory rhythm in mammals. *Science* 254: 726–729, 1991.

St.-John WM, and Paton JFR. Characterizations of eupnea, apneusis and gasping in a perfused rat preparation. *Respir Physiol* 123: 201–213, 2000.

Sun Q-J, Goodchild AK, Chalmers JP, and Pilowsky PM. The pre-Bötzinger complex and phase-spanning neurons in the adult rat. *Brain Res* 809: 204–213, 1998.

Tokumasu M, Nakazono Y, Ide H, Akagawa K, and Onimaru H. Optical recording of spontaneous respiratory neuron activity in the rat brain stem. *Jap J Physiol* 51: 613–9, 2001.

von Euler C. Brain stem mechanism for generation and control of breathing pattern. In: *Handbook of Physiology. The Respiratory System II: Control of Breathing*, edited by Chernack NS and Widdicombe JG. Washington, DC: American Physiological Society, 1986, p. 1–67.